J. Fluid Mech. (2005), *vol.* 536, *pp.* 401–421.
doi:10.1017/S0022112005004921 Printed in the United Kingdom

The stability of quasi-geostrophic ellipsoidal vortices

By DAVID G. DRITSCHEL, RICHARD K. SCOTT AND JEAN N. REINAUD

School of Mathematics and Statistics, University of St Andrews, St Andrews, UK

(Received 22 June 2004 and in revised form 1 March 2005)

A vertically standing freely-rotating ellipsoidal vortex of uniform anomalous *potential vorticity* in a rotating stratified fluid under quasi-geostrophic conditions of small Rossby and Froude numbers steadily rotates without change of form. The vortex can have arbitrary axis lengths, but must have one axis parallel to the vertical z-axis along the direction of gravity. The rotation rate is proportional to the potential vorticity anomaly but otherwise depends on only two independent aspect ratios characterizing the shape of the vortex. The linear stability of this class of vortex equilibria was first determined semi-analytically more than a decade ago. It was found that vortices are unstable over a wide range of the parameter space and are stable only when strongly oblate and of nearly circular cross-section.

New results, presented here, using a complementary approach and backed by nonlinear simulations of the full quasi-geostrophic equations indicate that these ellipsoidal vortices are in fact stable over a much wider range of parameter space. In particular, a mode previously thought to be unstable over much of the parameter space is evidently stable. Moreover, we have determined that this mode is just the difference between two neighbouring equilibrium states having slightly different horizontal aspect ratios; hence, this mode must be neutrally stable. Agreement is found for all other modes. However, by an independent analysis considering only ellipsoidal (though time-varying) disturbances, we have identified one unstable mode as purely ellipsoidal, i.e. it does not change the form of the ellipsoid, only its shape. Under this instability, the vortex quasi-periodically tilts over while undergoing mild changes in shape.

The range of parameters leading to non-ellipsoidal instabilities turns out to be narrow, with instability principally occurring for highly eccentric (horizontally squashed, prolate) vortices. The long-term fate of these instabilities is examined by nonlinear contour-dynamical simulations. These reveal a wealth of complex phenomena such as the production of a sea of small-scale vortices, yet, remarkably, the dominant vortex often tends to relax to a stable rotating ellipsoid.

1. Introduction

With recent improvements in both observations and simulations of the Earth's atmosphere and oceans, it has become evident that *vortices*, coherent masses of swirling fluid, play a major if not dominant role in the global circulation. Vortices are nonlinear manifestations of the high-Reynolds-number rotating stably-stratified fluid dynamics operating in these environments. They appear spontaneously, e.g. as instabilities, within the large-scale mean flow, and they are so numerous and energetic that they contribute strongly to the very mean flow they erupt from. Indeed, the large-scale circulations are thought to be 'eddy-driven', i.e. driven by vortices (Holton

et al. 1995; Garrett 2000). In the North Atlantic ocean alone, observations suggest that there are at least 10 000 vortices present in the surface layers (Ebbesmeyer *et al.* 1986), and with increasing resolution, numerical simulations of the global circulation are continually revealing more and longer-lived vortices (Siegel *et al.* 2001).

There are hence compelling reasons to understand better the behaviour of geophysical vortices. Perhaps the simplest pertinent model to do this is the *quasi-geostrophic* model, which applies for small Rossby and Froude numbers (strong background rotation and stratification). This model has become the workhorse of geophysical fluid dynamics, and its range of applicability appears to be significantly broader than strict asymptotics would indicate (cf. Dritschel & Viúdez 2003 and references therein). The quasi-geostrophic (QG) model filters relatively high-frequency inertia-gravity waves, leaving the (often) dominant vortical motions. The latter are fully controlled by the advection of a scalar field, the *potential vorticity* (PV), which is conserved following fluid elements in the absence of diabatic or dissipative processes.

In this work, we focus on the inviscid QG dynamics, and in particular investigate the stability of a class of vortex solutions discovered by Zhmur & Shchepetkin (1991) and Meacham (1992) and related to the 'gravitational ellipsoids' investigated by numerous mathematicians in the eighteenth and nineteenth centuries (see Chandrasekhar 1969 and references therein). They found that an ellipsoid, having arbitrary axis lengths and an arbitrary orientation, remains an ellipsoid for all time though the axis lengths and orientation generally vary in time. Certain special configurations simply rotate steadily about the vertical z-axis: (i) a vertically standing ellipsoid of arbitrary axis lengths, and (ii) a tilted spheroid (two axes of identical length, and the third tilted at an arbitrary angle with respect to the vertical). The stability – with respect to infinitesimal non-ellipsoidal perturbations – has been investigated for both configurations, with (i) the focus of Meacham (1992) and (ii) the focus of Miyazaki, Ueno & Shimonishi (1999).

Both analyses were semi-analytical, expanding perturbations in a finite series of special functions associated with an ellipsoid, then solving an eigenvalue problem numerically. Our own interest stems from the discovery that an entirely different approach, which we developed for arbitrary equilibrium vortex configurations (Reinaud & Dritschel 2002), does not agree fully with the results of Meacham (1992) for vertically standing ellipsoids. That our method agrees fully with the results of Miyazaki *et al.* (1999), with many of the other results presented in Meacham (1992), and with results obtained by integration of the full evolution equations using independent numerical techniques, indicates that our method is not flawed; but where our results differ is important, for instead of concluding that most vertically standing ellipsoids are unstable unless they have a nearly circular cross-section and are strongly oblate, we arrive at the conclusion that most such ellipsoids are stable except for highly eccentric (horizontally deformed and prolate) vortices.

The next section describes the basic set-up of the problem. Section 3 reviews our linear stability approach and presents a comprehensive picture of the stability properties over a wide range of the parameter space. In § 4, numerical simulations of the full QG equations are used to investigate the nonlinear consequences of the instabilities found and to explicitly verify the linear stability in the parameter range disputed. Finally, our conclusions are given in § 5.

2. Problem set-up

We consider an ellipsoid whose surface

$$\frac{x^2}{a^2} + \frac{y^2}{b^2} + \frac{z^2}{c^2} = 1 \tag{2.1}$$

encloses a region of non-zero uniform PV, $q=1$ without loss of generality, within an unbounded fluid. Here a, b and c are the semi-axis lengths. The evolution of the ellipsoid, under the QG approximation (cf. Gill 1982), is governed by the equations

$$\frac{\mathrm{D}q}{\mathrm{D}t} = q_t + u\,q_x + v\,q_y = 0, \tag{2.2}$$

$$\nabla^2\psi = \psi_{xx} + \psi_{yy} + \psi_{zz} = q, \tag{2.3}$$

$$u = -\psi_y, \quad v = \psi_x, \tag{2.4}$$

(subscripts x, y, z and t denote partial derivatives). Equation (2.2) expresses the material or pointwise conservation of PV on each isopycnal surface ($z=$ constant to leading order). Note that the flow is non-divergent. In (2.3), the height coordinate z has been stretched by the factor N/f, where N is the buoyancy frequency and f is the Coriolis frequency, both taken to be constant here. The resulting equations are independent of f and N, but formally apply only when these frequencies are large compared to the vertical and horizontal vorticity components, respectively.

Under the action of these dynamics, the ellipsoid (shape) rotates steadily about the z-axis, at a rate Ω depending only on two independent aspect ratios, $\alpha=a/c$, $\beta=b/c$. As c is the vertical semi-axis length, while a and b are the horizontal lengths, it proves convenient to work also with the horizontal aspect ratio $\lambda=a/b$ and the vertical aspect ratio $\mu=c/\sqrt{ab}$. Using a result originally due to Laplace (1784), it can be shown that

$$\Omega = \mu\frac{\lambda^{-1}R_D(\mu^2,\lambda,\lambda^{-1}) - \lambda R_D(\mu^2,\lambda^{-1},\lambda)}{3(\lambda^{-1}-\lambda)}, \tag{2.5}$$

where R_D is the elliptic integral of the second kind,

$$R_D(\xi,\eta,\zeta) = \tfrac{3}{2}\int_0^\infty \frac{\mathrm{d}t}{\sqrt{(t+\xi)(t+\eta)(t+\zeta)^3}}\,. \tag{2.6}$$

Figure 1 shows $\Omega(\alpha,\beta)$ and $\Omega(\lambda,\mu)$ over the range of parameters analysed in § 3 below. Ω increases with μ and λ, tending toward the two-dimensional limit of $\lambda/(1+\lambda)^2$ as $\mu\to\infty$. We may restrict attention to $\lambda\leqslant 1$ or $\alpha\leqslant\beta$ because of symmetry, but $\alpha>\beta$ is included also to compare directly with the results presented by Meacham (1992). An important point to note from figure 1 is the relative sizes of regions in parameter space: for example, oblate vortices occupy the regions $0<\mu<1$ and $\alpha\beta>1$. Thus, in the (α,β) view, the parameter space is dominated by increasingly oblate vortices.

3. Linear stability

3.1. *Approach*

Full details of the linear stability analysis are available in Reinaud & Dritschel (2002), so here we present only a brief sketch of the approach. The analysis was devised to treat general QG vortex equilibria consisting of one or more vortices, whose shapes are not known analytically, but must be found numerically. The single ellipsoidal vortex considered here is an exception, and it allows analytical progress to be made as regards linear stability. However, the algebra involved in the linear stability calculation is cumbersome and we have not been able to trace the apparent error in the analysis of Meacham (1992).

The approach we have taken, while more costly numerically, is nevertheless more straightforward. First, the ellipsoid is discretized into n_ℓ layers of equal thickness (40,

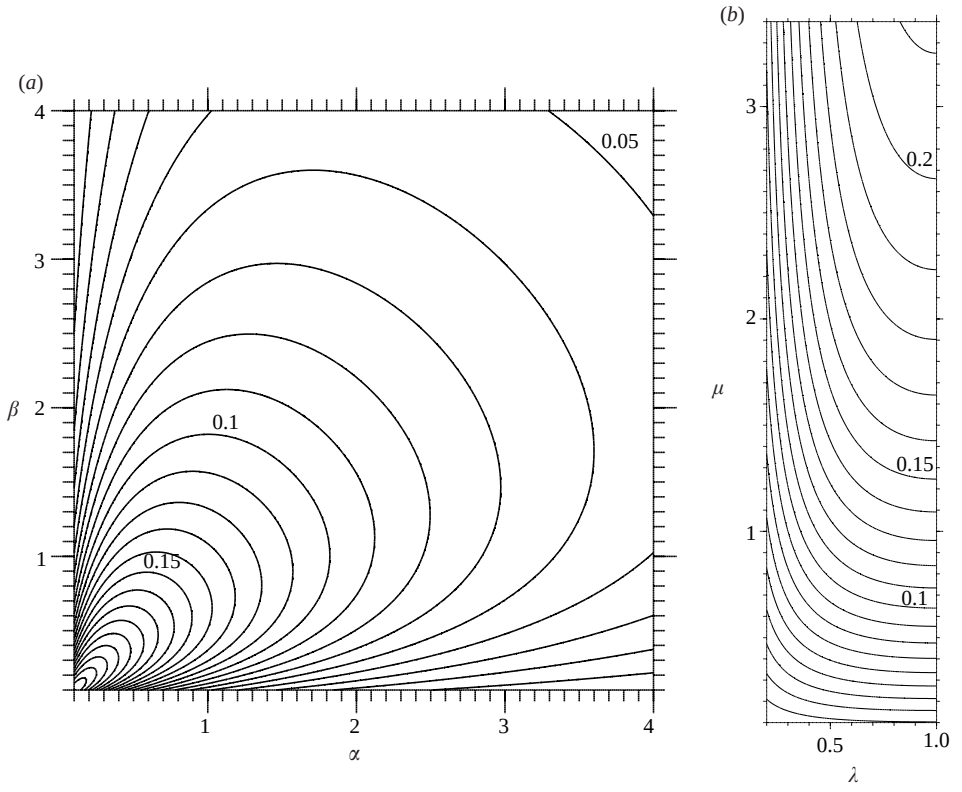

FIGURE 1. Rotation rate Ω of a free ellipsoidal vortex as (a) a function of α and β, and (b) as a function of λ and μ.

80 and 160 layers are used to check convergence). The layer thickness is $\Delta z = 2c/n_\ell$. Within each layer, we place the edge of the discrete vortex on the elliptical curve

$$\frac{x^2}{a^2} + \frac{y^2}{b^2} = r_k^2, \tag{3.1}$$

$k = 1, 2, \ldots, n_\ell$, where the r_k are chosen so that the volume containing PV in this layer, $\pi r_k^2 \Delta z$, is equal to the volume of the original ellipsoid within this layer. This gives

$$r_k^2 = 1 - \frac{\bar{z}_k^2}{c^2} - \frac{\Delta z^2}{12c^2}, \tag{3.2}$$

where $\bar{z}_k$ is the mean height of layer k.

Secondly, the ellipse is discretized into n_p points, with $n_p = 3n_\ell$ for high accuracy. The points are spaced equally in θ, such that $x = x_k \equiv a\, r_k \cos\theta$ and $y = y_k \equiv b\, r_k \sin\theta$. Using the fact that the flow field inside the ellipsoid is linear (cf. McKiver & Dritschel 2003), and the condition that the undisturbed vortex remains steady in a frame rotating at the rate $-\Omega$, it follows that $\mathrm{d}\theta/\mathrm{d}t = \Omega_{e,k}$ is constant along each ellipse. $\Omega_{e,k}$ is the angular velocity, in elliptical coordinates, of a particle moving around the ellipse in layer k (in general $\Omega_{e,k} \neq \Omega$, the rotation rate of the vortex shape). The constancy of $\Omega_{e,k}$ allows direct use of the linear disturbance equation, (7) in Reinaud & Dritschel (2002). This equation describes the evolution of a small-amplitude disturbance, expressed as an area displacement $\eta_k(\theta, t)$ of each elliptical

contour in each layer. Specifically, the disturbed contours have the form

$$(x, y) = (x_k, y_k) + \eta_k \frac{(\partial y_k/\partial\theta\,,\ -\partial x_k/\partial\theta)}{(\partial x_k/\partial\theta)^2 + (\partial y_k/\partial\theta)^2}. \tag{3.3}$$

Note that k corresponds to height, $z = \bar{z}_k$, and hence to a 'latitude' angle defined by $\phi = \sin^{-1}(\bar{z}_k/c)$.

Seeking an eigenform $\eta_k(\theta, t) = \mathrm{e}^{\sigma t}\hat{\eta}_k(\theta)$, we note that $\hat{\eta}_k(\theta)$ corresponds directly to the surface displacement $\Lambda(\theta, \phi)$ used by Meacham (1992), Miyazaki *et al.* (1999) and Hashimoto, Shimonishi & Miyazaki (1999). In the present analysis, the $\hat{\eta}_k$ are expanded in a truncated Fourier series

$$\hat{\eta}_k(\theta) = \sum_{m=1}^{M} A_m \cos m\theta + B_m \sin m\theta, \tag{3.4}$$

where $M = 5$ normally. Doubling M alters the results negligibly since the unstable modes primarily involve low m, in particular $m = 1$ according to the previously cited studies.

The main numerical cost is in evaluating the stability matrix. The eigenvalues σ are found by standard numerical routines. Instability corresponds to $\mathrm{Re}(\sigma) \equiv \sigma_r > 0$.

3.2. *Convergence*

A number of isolated parameter values were checked for numerical convergence. To be more thorough, we also checked an entire cross-section through parameter space, at a fixed horizontal aspect ratio of $\lambda = 1/2$, and the results are presented here. We varied the vertical aspect ratio μ from 0.1 to 4 in increments of 0.01, and performed stability analyses using $n_\ell = 40$, 80 and 160 layers.

The results are presented in figure 2, plotting the growth rate σ_r versus μ. As μ increases, so does the number of unstable modes, reaching 8 by $\mu = 4$. The principal or strongest instabilities correspond to the modes M2I, M3I, M4I and M5I of Meacham (1992), the first two of which are described there. The secondary instability erupting near $\mu = 1.8$ (not labelled) corresponds to M3III of Meacham (1992), while the others erupting near $\mu = 2.8$ and $\mu = 3.8$ appear to be higher-order modes (see below). The growth rates show little sensitivity beyond 80 layers and agree with those of Meacham (1992) as far as one can verify graphically (note Meacham scales his growth rates by 10^4). We know how to label the modes in figure 2 because the eigenfunctions shown in figure 3 agree with figures 4 and 9 of Meacham (1992) (for modes M2I and M3I; he does not show results for M4I and M5I). Note that these modes vary broadly in θ, and are dominated by $m = 1$ in (3.4). The eigenfunction of the secondary instability M3III also agrees with figure 13 of Meacham (1992). This, and the other two secondary instabilities (not shown) are dominated by $m = 2$, and have a meridional structure like M3I, M4I and M5I, respectively.

The small and diminishing mode seen at the bottom left of the plots in figure 2 is numerical – growth rates at $\mu = 0.7$ are $\sigma_r = 0.00379$ for $n_\ell = 40$, $\sigma_r = 0.00254$ for $n_\ell = 80$, and $\sigma_r = 0.00175$ for $n_\ell = 160$ – they decrease by a factor of approximately 0.68 on each doubling of n_ℓ. If we plot the eigenfunction for this mode at $\mu = 0.7$, see figure 4(*a*), we find the M2II mode of Meacham (1992), see his figure 6. However, according to his analysis, this mode is unstable with a growth rate of approximately $\sigma_r = 0.04$ at $\mu = 0.375$, and $\sigma_r = 0.015$ at $\mu = 0.7$. We believe this result is in error.

This mode, it turns out, corresponds to a rigid rotation of the original ellipsoid through a small angle ν about the vertical axis, i.e. into another steady ellipsoid, and hence is necessarily stable. A slight rotation of the ellipsoid generates new (x, y)

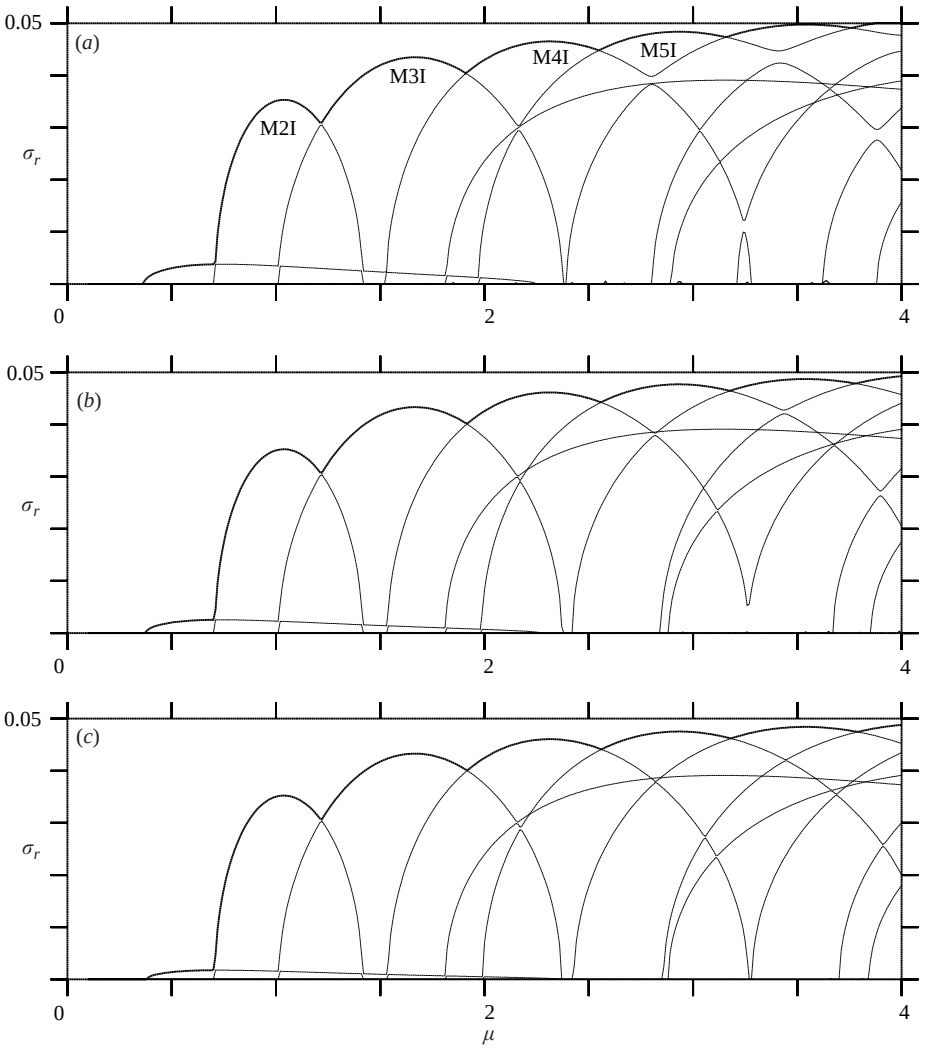

FIGURE 2. Growth rate as a function of vertical aspect ratio μ for $\lambda = 0.5$, and for (*a*) $n_\ell = 40$, (*b*) $n_\ell = 80$, and (*c*) $n_\ell = 160$. A bold line is used for the most unstable mode. The principle modes of instability, M2I ... M5I, are labelled in (*a*).

coordinates given by $x = x_k \cos \nu - y_k \sin \nu \approx x_k - \nu y_k$ and $y = y_k \cos \nu + x_k \sin \nu \approx y_k + \nu x_k$. Substituting these into (3.3) and solving for η_k (by projecting the disturbance onto $(\partial y_k/\partial\theta\,,\ -\partial x_k/\partial\theta)$ when $\nu \ll 1$) leads to

$$\eta_k(\theta, \phi) = -\tfrac{1}{2}\nu(b^2 - a^2)\cos^2\phi \sin 2\theta + O(\nu^2), \tag{3.5}$$

where $r_k = \cos\phi$ has been used. This eigenfunction is plotted in figure 4(*b*) next to the numerical eigenfunction in figure 4(*a*). The near perfect agreement further confirms that Meacham's mode M2II is spurious.

3.3. *Full results*

We next turn to the complete stability results over the two-dimensional parameter space investigated. For these results, we have used $n_\ell = 80$.

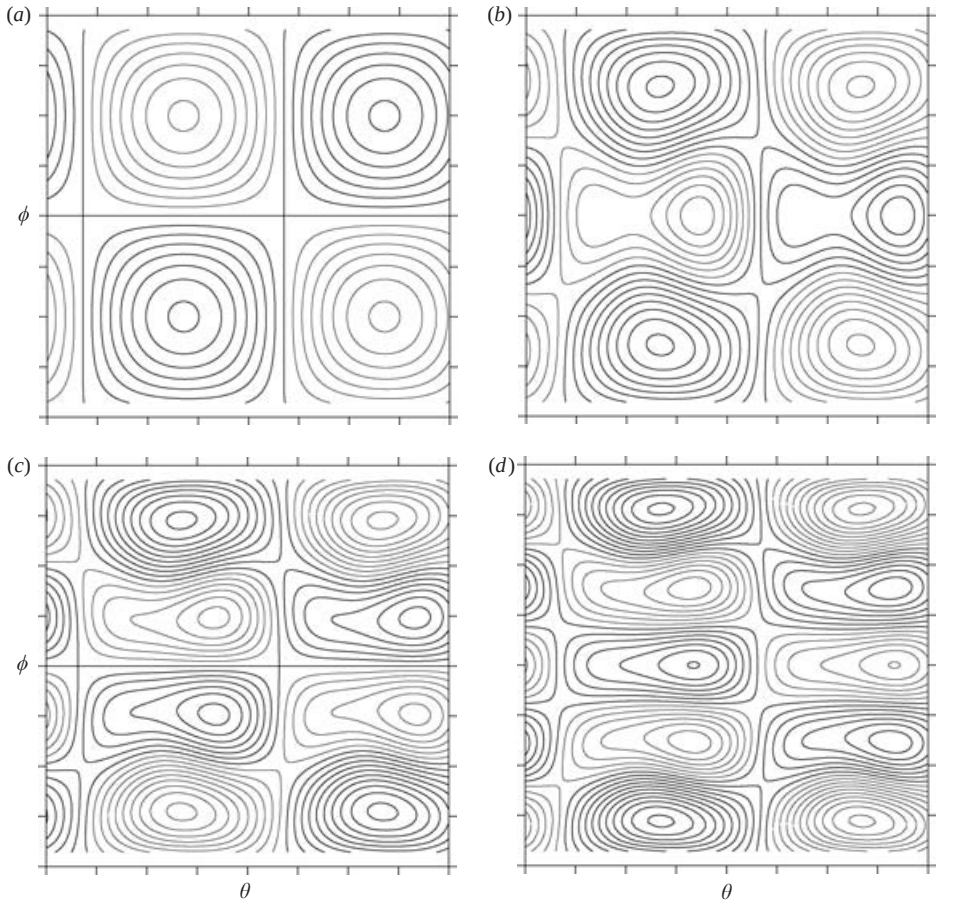

FIGURE 3. Eigenfunctions (*a*) M2I, (*b*) M3I, (*c*) M4I and (*d*) M5I plotted versus longitude θ ($-\pi \leqslant \theta \leqslant \pi$) and latitude ϕ ($-\pi/2 \leqslant \phi \leqslant \pi/2$), for $\lambda = 0.5$ and for the most unstable vertical aspect ratios, $\mu = 1.04$, 1.67, 2.31 and 2.93, respectively. The contour interval is 0.1 and the eigenfunctions have unit r.m.s. values. Bold contours show positive or zero values.

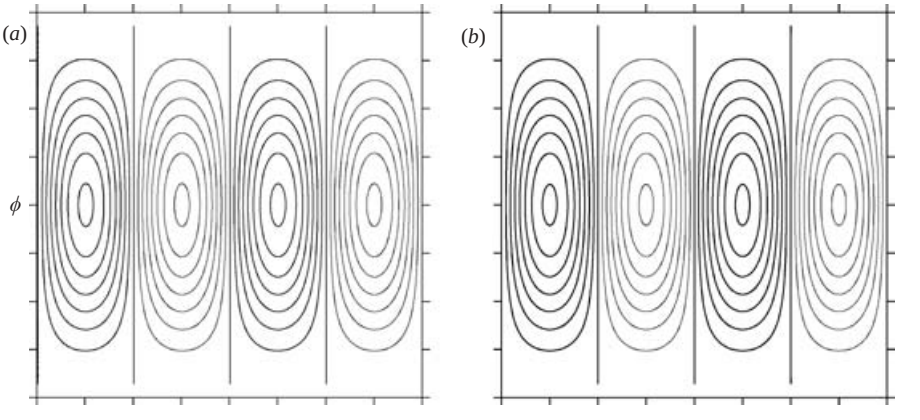

FIGURE 4. (*a*) Eigenfunction M2II at $\mu = 0.7$ and $\lambda = 0.5$, in the same format as the previous figure. (*b*) The exact, analytical form of this eigenfunction (see text).

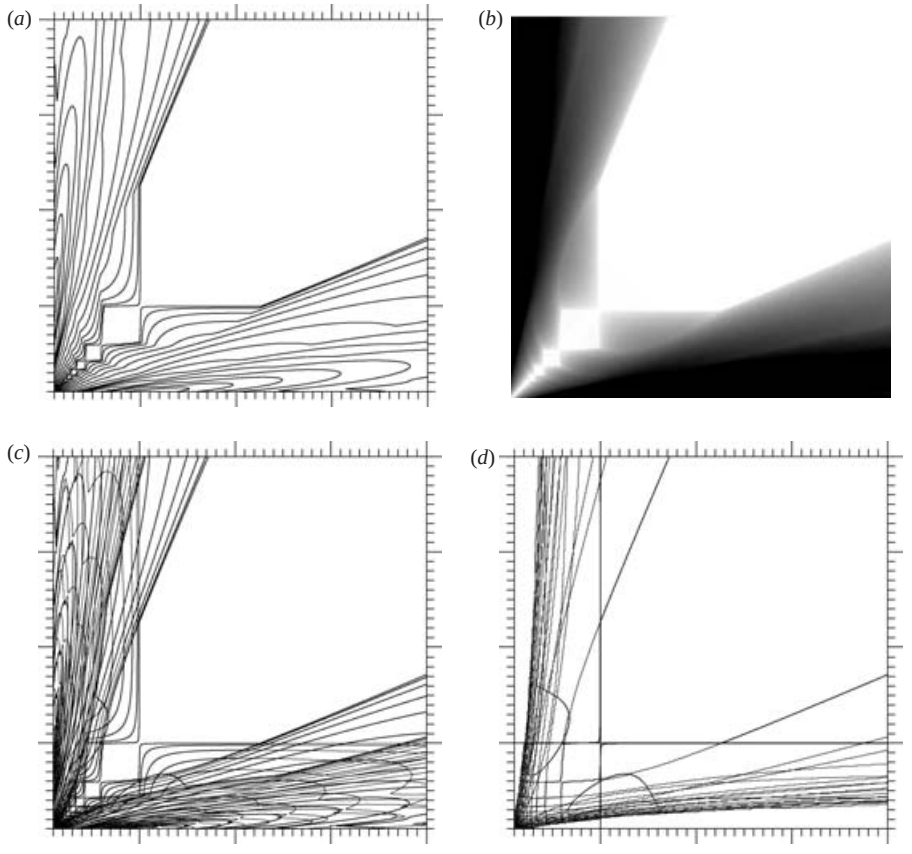

FIGURE 5. Domain of instability in the parameter space (α, β): (*a*) contours of maximum growth rate σ_r at the levels $\sigma_r = 0.002$, 0.01, 0.02, etc.; (*b*) σ_r shaded, with the darkness proportional to growth rate (all growth rates greater than 0.1 are solid black); (*c*) the three most unstable modes superposed; (*d*) the near marginal contours (at $\sigma_r = 0.002$) for the 20 most unstable modes. Tick marks in α and β are placed every 0.1 units, from 0.1 to 4. Double length tick marks are placed at α and $\beta = 1$, 2, 3 and 4.

The results are displayed in two ways, first in the format used by Meacham (1992), with the growth rate σ_r expressed as a function of $\alpha = a/c$ and $\beta = b/c$, over the ranges $0.1 \leqslant \alpha \leqslant 4$ and $0.1 \leqslant \beta \leqslant 4$ (in increments of $\Delta\alpha = \Delta\beta = 0.01$), and second with σ_r expressed as a function of $\lambda = a/b$ and $\mu = c/\sqrt{ab}$, over the ranges $0.2 \leqslant \lambda \leqslant 1$ and $0.1 \leqslant \mu \leqslant 3.4$ (in increments of $\Delta\lambda = \Delta\mu = 0.01$).

Figure 5 shows $\sigma_r(\alpha, \beta)$, in several formats. Figures 5(*a*) and 5(*b*) show the maximum growth rate as contours and as a shaded diagram. Figure 5(*c*) shows the three most unstable modes superposed and figure 5(*d*) shows the margin of stability for the first 20 modes. A striking feature is the almost geometric sequence of shrinking domains of stability as $\alpha \sim \beta \to 0$, i.e. for increasingly prolate vortices. In fact, there is an infinite sequence arising from a weak resonant instability of modes MjI, $j = 2, 3, 4, \ldots$, for vortices having a nearly circular horizontal cross-section at the values $\alpha = \beta = 1$, 0.59129658, 0.42623214, etc., see Miyazaki *et al.* (1999) and table 1. Analogous parametric instabilities occur for a strained two-dimensional elliptical vortex (Moore & Saffman 1971; Dritschel 1990) and for homogeneous (unstratified) flow in a rigid ellipsoidal container (cf. Kerswell 2002 and references therein).

j	α	μ
2	1.00000000	1.00000000
3	0.59129658	1.69119870
4	0.42623214	2.34613938
5	0.33565913	2.97921288
6	0.27781562	3.59950966
7	0.23743331	4.21170902
8	0.20753601	4.81844096
9	0.18445758	5.42130077
10	0.16607670	6.02131440

TABLE 1. Resonant values of α and $\mu = 1/\alpha$ for a vortex of circular cross-section $\alpha = \beta$ or $\lambda = 1$. Here, j is the primary mode index for modes MjI.

This way of depicting the domain of instability emphasizes oblate vortices ($\alpha\beta > 1$), for which instability is largely confined to strongly deformed, horizontally elongated vortices with $\alpha/\beta \lesssim 0.42$ or $\beta/\alpha \gtrsim 2.4$, and squashes all prolate vortices into the lower and left edges of the figure. An alternative view, plotting σ_r as a function of the horizontal and vertical aspect ratios, λ and μ, shows that each primary mode MjI occupies a roughly equal area of instability, see figure 6. The gravest mode, M2I, is the least prolate and stems from the point $\lambda = \mu = 1$ (a spherical vortex). This mode, like the neutral M2II mode discussed above, can be shown to be an ellipsoidal disturbance. The difference is that the M2I mode tilts the ellipsoid so that no axis is vertical. This has been found independently by a much simpler stability analysis restricted to ellipsoidal disturbances (McKiver 2003; Reinaud & Dritschel 2005). This simple analysis gives a domain of instability for M2I that matches in detail the domain found using the full analysis described above – see figure 6(c). Further, it also finds the purely ellipsoidal mode M2II to be neutrally stable.

The nonlinear evolution of the M2I instability is discussed more fully below, but it is important to remark here that this instability preserves the ellipsoidal shape of the vortex, merely affecting the orientation of the vortex's axes. While this gives rise to a time-dependent motion of the vortex, with near recurrence of the initial state, it does not change the basic vortex characteristics. In short, it is not an important instability. All other modes are non-ellipsoidal, and may be expected to lead to significant changes, as the results of the next section bear out. The main implication of these results is that isolated oceanic vortices are stable over a much larger region of parameter space than was argued by Meacham (1992). In particular, oblate vortices are generally stable except when strongly horizontally elongated.

4. Nonlinear evolution

To investigate the nature of the instabilities described in the previous section, several representative nonlinear simulations of the vortex evolution in the fully nonlinear QG equations (2.2)–(2.4) were performed (see table 2). We used the CASL algorithm, a numerical method combining contour dynamics with standard spectral methods (Dritschel & Ambaum 1997). This is ideally suited, apart from the need to confine the flow to a triply-periodic box, since it allows us to deal with discontinuities in PV naturally and with minimal numerical dissipation. To reduce periodicity effects, we ensure that the vortex occupies no more than a small fraction, between 0.014 and 0.16 % of the domain volume (following the guidelines in Reinaud & Dritschel 2002).

λ	μ	n_ℓ	$\bar{\delta}_E$
1/3	1/3	80	0.0544
2/5	2/5	80	0.0533
4/9	4/9	80	0.00953
2/5	2/3	80	0.0648
1/2	1	80	0.0635
1/2	4/3	80	0.0627
1/2	2	120	0.0750
2/3	1	80	0.00565
2/3	1.6912	120	0.0932
2/3	2.3461	160	0.0785
2/3	2.9792	160	0.0621

TABLE 2. Summary of the nonlinear simulations, giving the initial ellipsoidal parameters λ and μ, the number of layers spanning the vortex n_ℓ, and the mean departure of the vortex from an ellipsoid $\bar{\delta}_E$ (see text) over $150 \leqslant t \leqslant 200$.

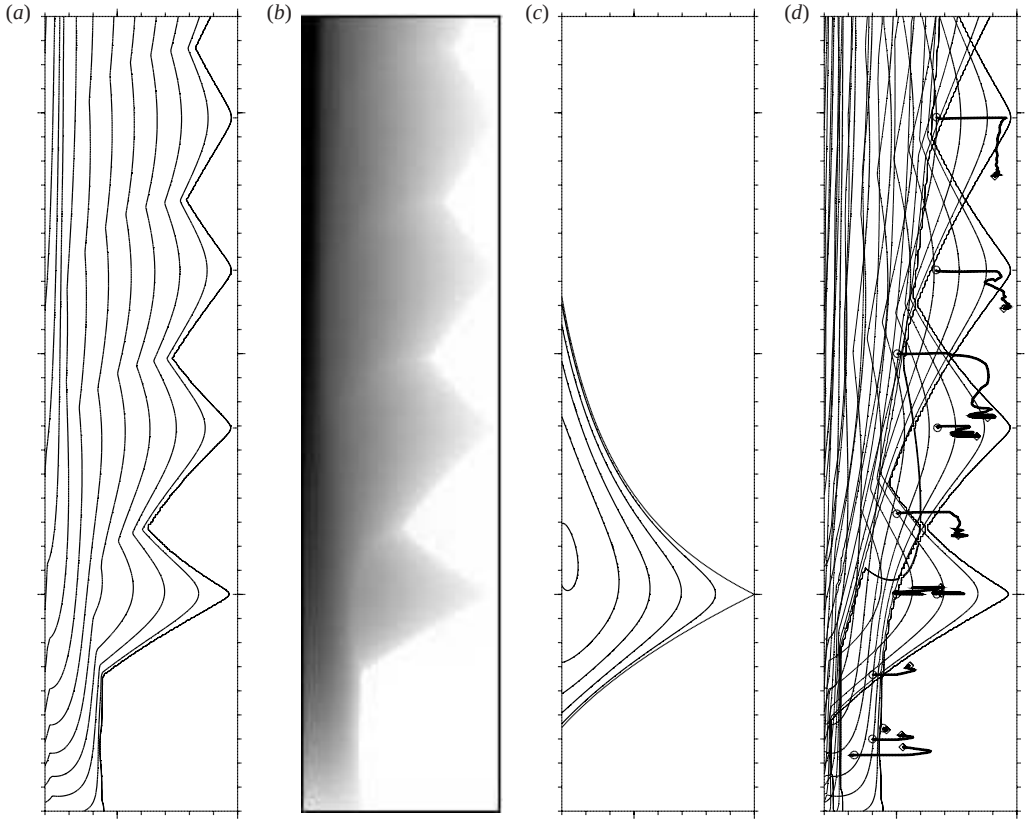

FIGURE 6. Domain of instability in the parameter space (λ, μ): (*a*) contours of maximum growth rate σ_r at the levels $\sigma_r = 0.002$, 0.01, 0.02, etc.; (*b*) σ_r shaded, with the darkness proportional to growth rate (all growth rates greater than 0.1 are solid black); (*c*) σ_r for the purely ellipsoidal mode starting from $\sigma_r = 0$ (see text); (*d*) the three most unstable modes superposed (the extra thick lines are the result of nonlinear simulations, described in § 4). Tick marks in λ and μ are placed every 0.1 units, for $\lambda \in [0.2, 1]$, and for $\mu \in [0.1, 3.4]$. Double length tick marks are placed at $\lambda = 0.5$ and 1, and at $\mu = 1$, 2 and 3.

Each simulation uses a basic grid of 256^3 for solving the Poisson equation, (2.3), and for representing the velocity field; however, a grid four times finer in each direction is used to represent the gridded PV obtained from the contours, for high accuracy (see Dritschel & Ambaum 1997). Within the 1024 vertical layers available, in most cases the vortex is taken to be 80 layers deep, but more layers are used for highly prolate vortices to ensure adequate vertical resolution (see table 2). Other parameter settings are standard: a large scale length L equal to the mean horizontal radius of the vortex, a surgical scale equal to a twentieth of the basic grid size, and a time step $\Delta t = T/40$, where $T \equiv 4\pi/Q$ and Q is the uniform PV within the vortex. For the results shown below, time t is scaled on T. All simulations extend to $t = 200$ though most of the action takes place early on, before $t = 100$, and over a relatively short time period, 10 to 20 time units.

As a diagnostic, we compute the ellipsoidal moments of the evolving vortex. At each time saved (every 0.5 units), the vortex (or the biggest vortex in cases where it loses material) was fit to an ellipsoid having the same volume V, centre $\boldsymbol{X}$, and second moments B_k, $k = 1, 2, \ldots, 6$, defined by

$$\left.\begin{aligned} B_1 &= \frac{5}{V}\iiint_V x^2\,\mathrm{d}V, \quad B_2 = \frac{5}{V}\iiint_V xy\,\mathrm{d}V, \quad B_3 = \frac{5}{V}\iiint_V xz\,\mathrm{d}V, \\ B_4 &= \frac{5}{V}\iiint_V y^2\,\mathrm{d}V, \quad B_5 = \frac{5}{V}\iiint_V yz\,\mathrm{d}V, \quad B_6 = \frac{5}{V}\iiint_V z^2\,\mathrm{d}V, \end{aligned}\right\} \tag{4.1}$$

where x, y, z are coordinates relative to the vortex centre (McKiver & Dritschel 2003; Dritschel, Reinaud & McKiver 2004). Initially, $B_1 = a^2$, $B_4 = b^2$, $B_6 = c^2$ and $B_2 = B_3 = B_5 = 0$. Tracking the evolution of these moments allows us to quantify the changes to the basic vortex characteristics as a result of instability, in particular the changes in λ and μ. To measure how good the fit to an ellipsoid is, the departure ϵ of each point $\boldsymbol{x} = (x, y, z)$ on the surface of the vortex from the fitted ellipsoid is computed, and its root mean square δ_E is found. The local departure ϵ is determined by solving the cubic equation

$$\frac{\tilde{x}^2}{\epsilon + a^2} + \frac{\tilde{y}^2}{\epsilon + b^2} + \frac{\tilde{z}^2}{\epsilon + c^2} = 1, \tag{4.2}$$

where a, b and c are the vortex semi-axis lengths ($a \leqslant b \leqslant c$), and where $\tilde{\boldsymbol{x}}$ are centroid-relative coordinates in which $\epsilon = 0$ gives the boundary of the ellipsoid. In general, there may be three real roots, and we choose the smallest (in magnitude) for which $\epsilon \geqslant -a^2$. We note that ϵ spans a family of confocal ellipsoids (see Appendix B of Dritschel *et al.* 2004), the innermost being an elliptic sheet when $\epsilon = -a^2$. The mean square departure δ_E^2 is found by integrating ϵ^2 with respect to arclength s around each contour, then normalizing the result by the total arclength multiplied by $r_E^2 \equiv (a^2 + b^2 + c^2)/3$:

$$\delta_E^2 = \frac{\displaystyle\sum_{\ell=1}^{n_\ell} \oint_{C_\ell} \epsilon^2 \mathrm{d}s}{r_E^2 \displaystyle\sum_{\ell=1}^{n_\ell} \oint_{C_\ell} \mathrm{d}s}. \tag{4.3}$$

Above, C_ℓ is the contour belonging to the vortex in layer ℓ. All contour integrations (including those involved in the calculation of the second moments B_k after conversion to contour integrals) are performed using two-point Gaussian quadrature between contour nodes.

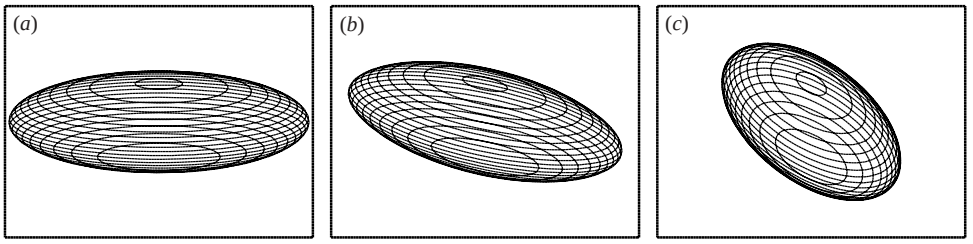

FIGURE 7. Nonlinear evolution of a vortex, initially an ellipsoid with $\lambda = 4/9$ and $\mu = 4/9$, at times (*a*) $t = 0$, (*b*) 100 and (*c*) 200, viewed in orthographic perspective at an angle of 60° from the vertical in the (y, z)-plane. In this and all subsequent images of vortex evolution, only the contours in every third layer are shown (here, the vortex spans 80 layers).

We begin by examining oblate vortices ($\mu < 1$), and contrast an M3I-unstable case ($\lambda = \mu = 2/5 = 0.4$; $\sigma_r = 0.0215$) with a nearby stable case ($\lambda = \mu = 4/9 \approx 0.444$) marked by the open circles in the lower part of figure 6(*d*). According to Meacham (1992), the latter is unstable to M2II (with growth rate $\sigma_r \approx 0.036$). The vortex evolutions (in a frame rotating with the equilibrium rotation rate) are contrasted in figures 7 and 8. The stable case remains virtually unchanged over the long duration of the simulation, apart from a weak rotation induced by periodicity (the second moments change by less than 4 %, the angle between the minor axis and the vertical remains less than 0.002°, and $\delta_E < 0.0123$). By contrast, the unstable case develops an 'egg' shape characteristic of the linear eigenmode (cf. figure 3(*a*)) which subsequently distorts into a large filament spun off from the vortex mid-section, leaving it with a nearly vertical edge there. During this part of the instability, δ_E increases to over 1.57. The filament then rolls up into a multitude of smaller vortices (together constituting 2.5 % of the original vortex volume) which orbit the main vortex. Upon fitting the vortex to an ellipsoid, we find that the shape characteristics vary little following the detachment of the filament, see figure 9, and moreover that the vortex is approximated well by an ellipsoid in this later period ($\bar{\delta}_E = 0.0533$ over the last 50 time units). Similar behaviour has been found for other unstable oblate vortices: the initial formation of a single filament from the vortex mid-section followed by its detachment and the consequent reduction of the width of the main vortex.

For all cases investigated, in fact, we have found that the original vortex settles down to another roughly ellipsoidal steadily-rotating vortex ($\bar{\delta}_E < 0.1$) with well-defined values of λ and μ. Trajectories showing the evolution of these parameters are drawn in figure 6(*d*) – see the thick bold curves originating from the small circles and ending at the diamonds. In all cases, the vortex ends up in a stable part of the parameter space, or in one which is weakly unstable (for λ close to 1), or in a part which is unstable to ellipsoidal disturbances (mode M2I) only.

We turn next to the ellipsoidal instabilities, the parameter range unstable to M2I (see figure 6(*c*)). Two cases are examined. In the first ($\lambda = 2/3$, $\mu = 1$; $\sigma_r = 0.0222$) the vortex is M2I-unstable only. The evolution of the vortex is shown in figure 10, qualitatively confirming that the vortex remains ellipsoidal. In figure 6, the shape of the vortex (λ, μ) does not evolve significantly, and in particular remains in the M2I-unstable part of the parameter space. The vortex quasi-periodically tilts over (the original vertical axis tilts through the (x, y)-plane), tumbles and nearly recovers its initial condition. This is not destructive.

To quantify this behaviour, we compare it next with the purely ellipsoidal evolution, computed using the 'ellipsoidal model' (McKiver & Dritschel 2003; Dritschel

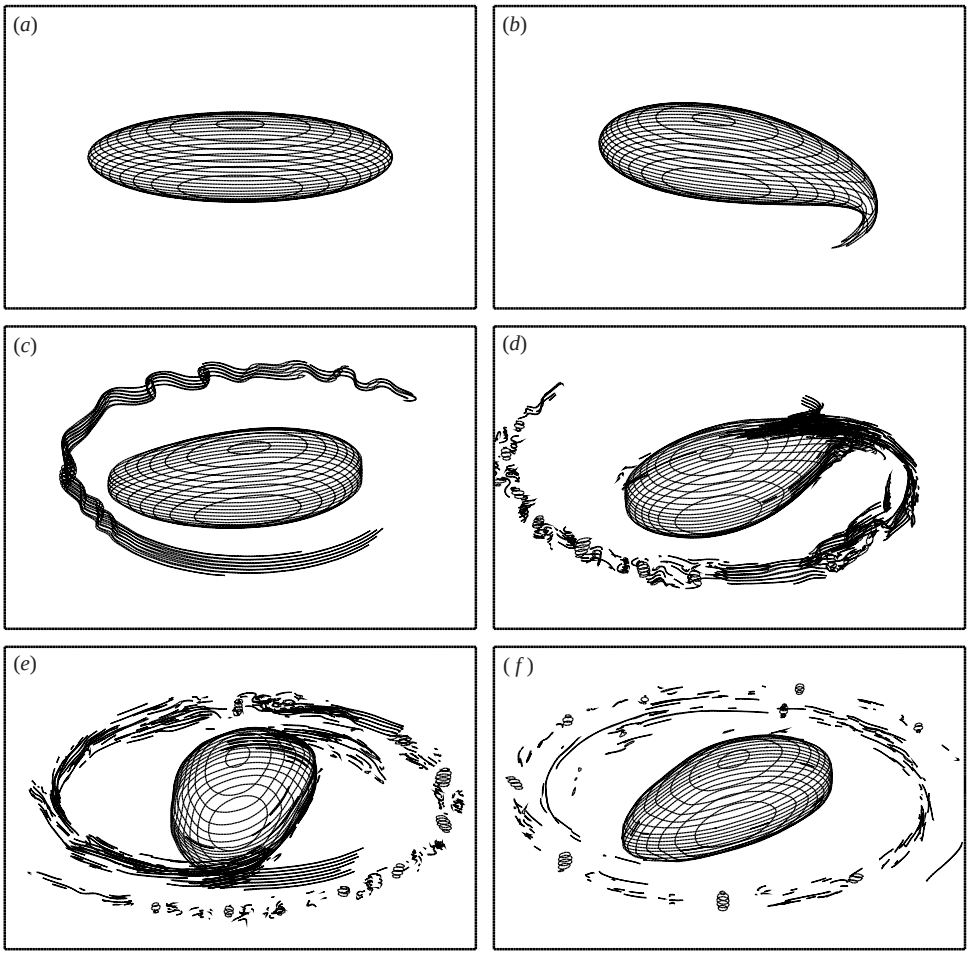

FIGURE 8. Nonlinear evolution of a vortex, initially an ellipsoid with $\lambda = 2/5$ and $\mu = 2/5$, from (a) to (f) at times $t = 0$, 48, 56, 64, 72 and 100, viewed in the same perspective as in figure 7.

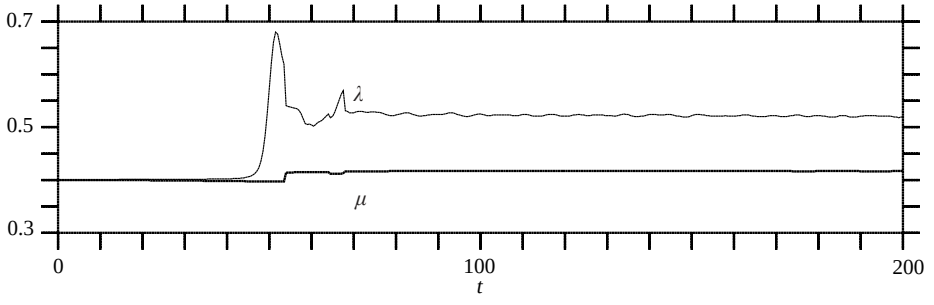

FIGURE 9. Evolution of the ellipsoidal parameters λ and μ for the simulation shown in figure 8.

et al. 2004). The ellipsoidal model exploits the fact that an isolated ellipsoid remains an ellipsoid for all time under QG dynamics, governed by (2.2)–(2.4). The full CASL numerical simulations introduce non-ellipsoidal disturbances by way of the vertical discretization of the vortex into layers, so the comparison is not trivial.

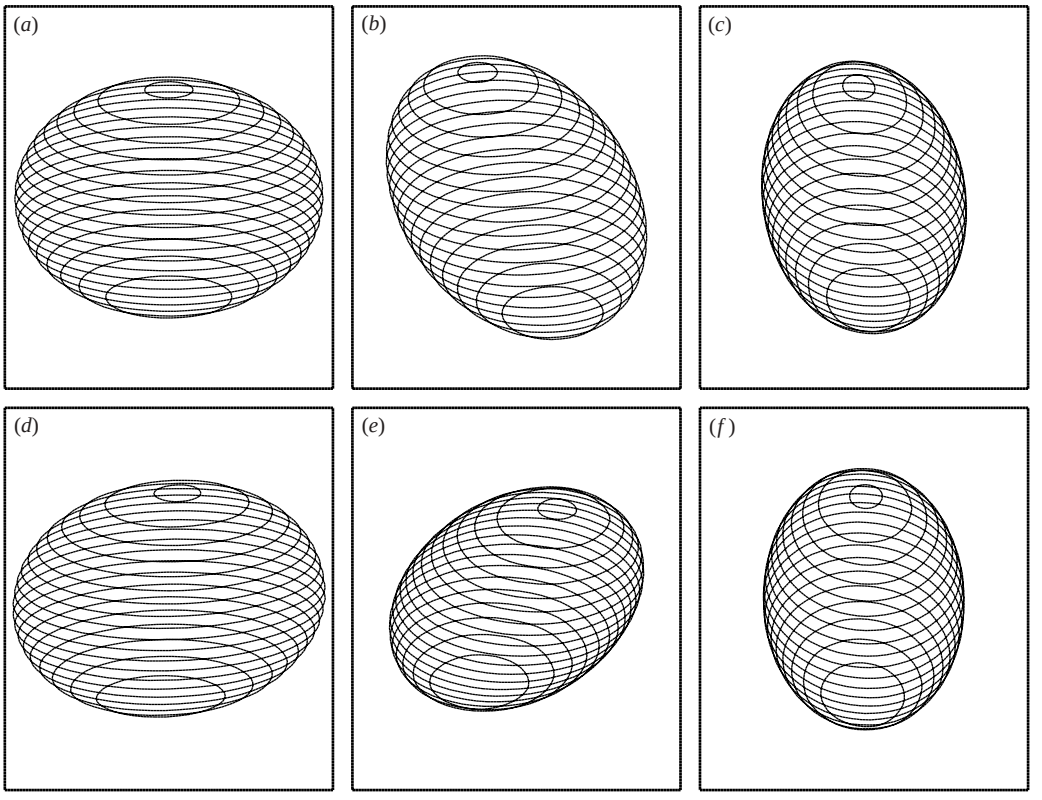

FIGURE 10. Nonlinear evolution of a vortex, initially an ellipsoid with $\lambda = 2/3$ and $\mu = 1$, from (a) to (f) at times $t = 0$, 45, 54, 82, 91 and 100, viewed in the same perspective as in figure 7.

Under the purely ellipsoidal dynamics, the semi-axis lengths a, b, c of the vortex remain constant (the vortex shape remains unchanged) as it tumbles in the M2I instability. The axis orientations vary, yet the fluid motion is still horizontal or layerwise two-dimensional. To check the constancy of a, b, c in the CASL simulation, the vortex is fit to an ellipsoid at each time t to extract $a(t)$, $b(t)$, $c(t)$. The discrepancy from the initial ellipsoidal shape

$$[(a-a_0)^2 + (b-b_0)^2 + (c-c_0)^2]^{1/2} / \left(a_0^2 + b_0^2 + c_0^2\right)^{1/2},$$

where $a_0 = a(0)$ etc, is never more than 0.017 (and decreases after $t = 100$), and the r.m.s. discrepancy over all time is 0.012, i.e. about 1 %.

A direct comparison between the CASL simulation and the ellipsoidal dynamics has also been performed by comparing the second moments B_k, $k = 1, 2, \ldots, 6$ in (4.1) diagnosed from the CASL simulation with those evolved under the ellipsoidal dynamics. Since the instability grows from numerical noise, the comparison was carried out starting from two later times near the onset of instability (the CASL-diagnosed moments were used to initialize the ellipsoidal model). The evolution of the initially zero moments B_3 and B_5 is shown in figure 11, for the CASL simulation (figure 11a), and the ellipsoidal model starting from $t = 30$ (figure 11b) and $t = 56$ (figure 11c). Starting from $t = 30$, the ellipsoidal model captures the first peak in the moments to within 0.8 % of their magnitude, but fails to capture the second peak. This is evidently due to extra noise in the CASL simulation that stimulates further

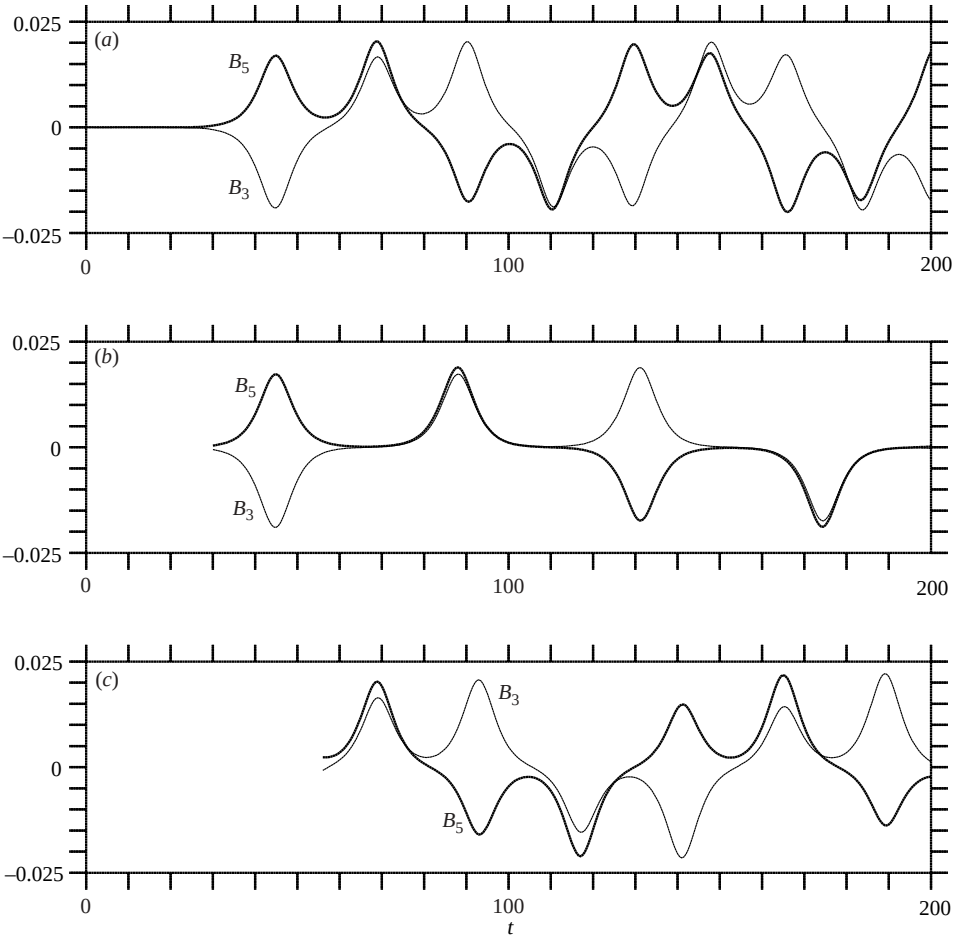

FIGURE 11. Time evolution of the second-order ellipsoidal moments B_3 and B_5 for (a) the full QG dynamics, and (b, c) the ellipsoidal model, (b) initialized with the moments obtained from the full dynamics at $t = 30$ and (c) $t = 56$.

tumbling of the vortex. Starting from $t = 56$, the ellipsoidal model now captures this second peak with comparable accuracy, as well as the subsequent general behaviour. Given the differences in the two models, and the strong nonlinearities of the evolution, we cannot expect close agreement for all time.

Finally, in the CASL simulation, the departure of the vortex from an ellipsoid δ_E is never greater than 0.00673, more than two orders of magnitude smaller than the maximum δ_E found in simulations of other unstable vortices (see figure 12). Similarly, small values of δ_E are found for the stable vortex $\lambda = \mu = 4/9$ pictured in figure 7.

Consider next a vortex with a smaller horizontal aspect ratio $\lambda = 1/2$ (still for $\mu = 1$), which lies on the margin of stability for M3I and well within the M2I-unstable region (with $\sigma_r = 0.0350$). The evolution is shown in figure 13. The vortex first tilts, tumbles and recovers (nearly twice) before destabilizing to M3I. The long filament which forms around $t = 54$ induces a large departure from an ellipsoidal shape (see figure 12b). The smaller filament ejected around $t = 125$ (now near the top of the vortex) also induces a couple of local peaks in δ_E (the second peak comes from the brief re-entrainment of the filament around $t = 130$). Thereafter δ_E remains small and the

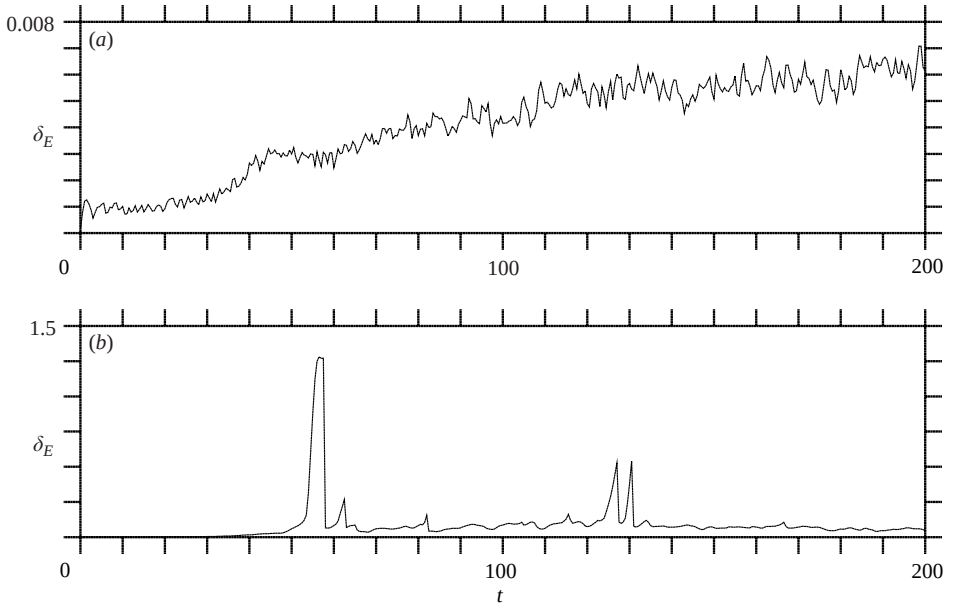

FIGURE 12. Time evolution of the departure from an ellipsoidal shape δ_E for (*a*) $\lambda = 2/3$ and $\mu = 1$ (M2I unstable) and (*b*) $\lambda = 1/2$ and $\mu = 1$ (M2I and marginally M3I unstable).

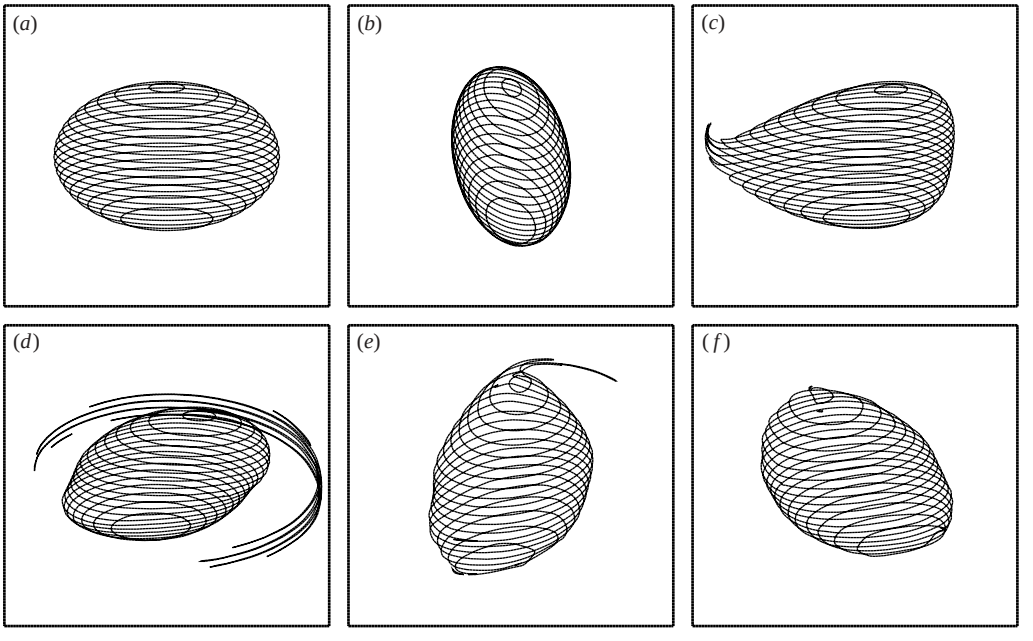

FIGURE 13. Nonlinear evolution of a vortex, initially an ellipsoid with $\lambda = 1/2$ and $\mu = 1$, from (*a*) to (*f*) at times $t = 0$, 35, 54, 58, 125 and 183, viewed in the same perspective as in figure 7.

vortex is approximated well by an ellipsoid. In this case, the vortex shape parameters λ and μ evolve away from the M3I stability boundary, but end up in the M2I-unstable part of the parameter space.

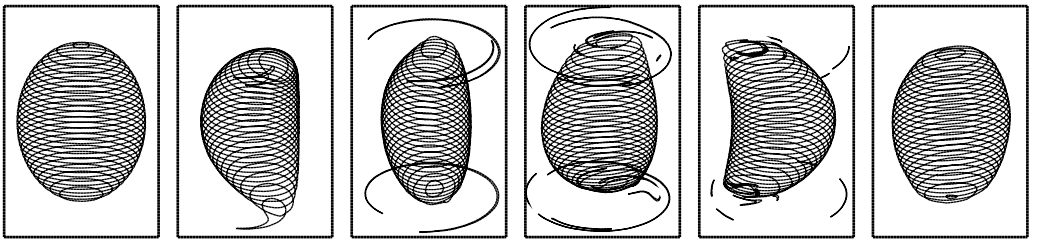

FIGURE 14. Nonlinear evolution of a vortex, initially an ellipsoid with $\lambda = 2/3$ and $\mu = 1.6912$, from left to right at times $t = 0$, 50, 55, 67, 80 and 200, viewed in the same perspective as in figure 7.

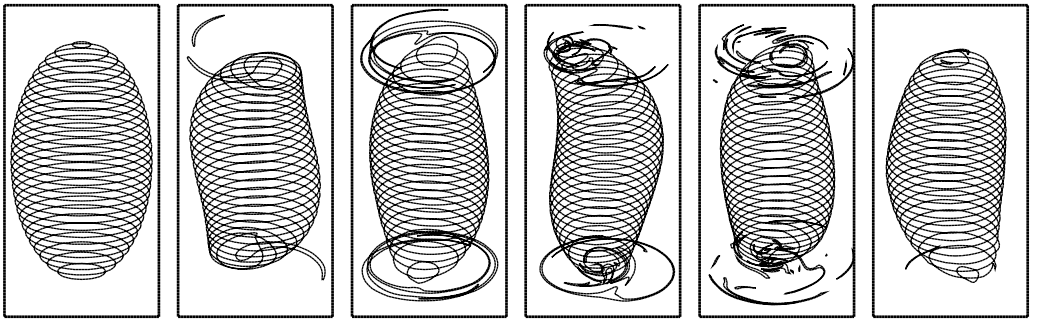

FIGURE 15. Nonlinear evolution of a vortex, initially an ellipsoid with $\lambda = 2/3$ and $\mu = 2.3461$, from left to right at times $t = 0$, 24, 34, 45, 60 and 200, viewed in the same perspective as in figure 7.

As we consider increasingly prolate vortices, the instabilities tend only to tear off the top and bottom of the vortex, thereby decreasing μ (and increasing λ toward 1). For example, the case in the middle-part of the M3I instability region ($\lambda = 2/3$, $\mu = 1.6912$; $\sigma_r = 0.0271$; see figure 6) destabilizes by throwing off filaments at the top and bottom of the vortex (in phase), see figure 14. The instability first makes the vortex mid-section more circular, and, in order to conserve angular impulse

$$J = \iiint (x^2 + y^2)\mathrm{d}V = \frac{1}{5}V(B_1 + B_4), \tag{4.4}$$

the upper and lower parts of the vortex (which have a smaller cross-sectional area) must drift away from the z-axis. Advection then twists these extremities into spiralling filaments which eventually detach from the main vortex.

Similar behaviour is exhibited in the case of the M4I instability ($\lambda = 2/3$, $\mu = 2.3461$; $\sigma_r = 0.0289$) shown in figure 15. A qualitative difference is that the filaments are ejected 180° out of phase, consistent with the eigenfunction shown in figure 3(*b*). The M5I instability ($\lambda = 2/3$, $\mu = 2.9792$; $\sigma_r = 0.0299$) – see figure 16 – is again like M3I, and so on. This appears to be a simple consequence of the respective symmetries of the odd and even modes, see figure 3. Modes MjI with j odd are all symmetric in z, while modes with j even are all anti-symmetric.

The key point is that all of these instabilities result in roughly ellipsoidal stable vortices (stable, that is, to non-ellipsoidal disturbances). The true domain of stability, if we exclude the M2I instability, is much wider than was previously thought – significantly deformed vortices having $\mu = O(1)$ or less are robust, not only to linear

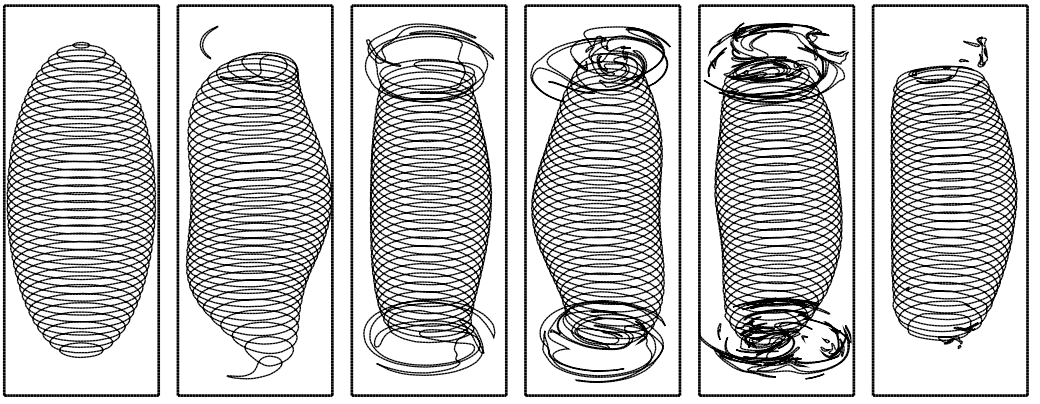

FIGURE 16. Nonlinear evolution of a vortex, initially an ellipsoid with $\lambda = 2/3$ and $\mu = 2.9792$, from left to right at times $t = 0$, 31, 40, 47, 60 and 179, viewed in the same perspective as in figure 7.

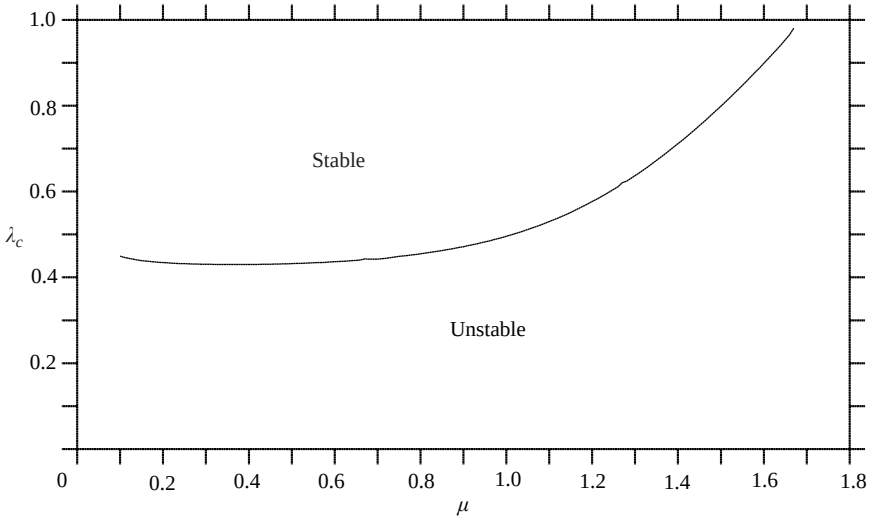

FIGURE 17. The stability boundary $\lambda = \lambda_c(\mu)$ for non-ellipsoidal disturbances, and for vortices having a height–width aspect ratio $\mu \leqslant 1.67$.

perturbations, but apparently also to weakly nonlinear ones. Some more prolate vortices are stable as well, but the windows of stability shrink with increasing μ and stability is found only close to $\lambda = 1$. The chief domain of stability, however, is found for $\mu < 1.6912$, and is bounded by the margin of stability for M3I, i.e. for $\lambda > \lambda_c(\mu)$ – see figure 17. Here, we have determined λ_c by fitting σ_r^2 to a quadratic polynomial in λ using three successive unstable values of λ near the margin of stability.

5. Conclusions

We have revisited a basic problem in the stability of geophysical vortices in a rotating, stratified fluid. In the original study, Meacham (1992) concluded that a wide class of vortices, of ellipsoidal shape, are unstable. Stability was found only for vortices of nearly circular horizontal cross-section or of small height to mean-width aspect

ratio (after the usual stretching of the vertical coordinate z by N/f, the buoyancy to Coriolis frequency ratio).

Here, by an alternative and direct stability analysis, we have found that the region of stability is much wider than previously thought, with stability existing over a wide range of commonly observed vortex shapes (Reinaud *et al.* 2003). In particular, vortices of order unity height to mean-width aspect ratio μ are stable, in the sense that they preserve their ellipsoidal shape, unless the horizontal aspect ratio λ is significantly smaller than unity. There exists a range of parameters 'unstable' purely to ellipsoidal disturbances, but then the vortex simply tumbles while preserving its shape and axis lengths. Beyond this domain, there exist completely linearly stable domains, for both prolate $\mu > 1$ and oblate $\mu < 1$ vortices, previously found to be unstable. The spurious mode turns out to be just the difference between two equilibrium ellipsoids of slightly different λ.

These linear results have been backed up by a series of numerical simulations of the nonlinear quasi-geostrophic governing equations. The simulations confirm our linear stability results, in particular the newly found stable parameter regimes, and illustrate the range of behaviour occurring for unstable vortices to late times. In every case examined, despite significant ejections of material from the vortex and associated complex nonlinear behaviour, the main vortex returns and remains close to an evidently stable ellipsoidal form, albeit not always a steadily rotating one. Moreover, in each case, the main vortex loses no more than a few per cent of its volume. These instabilities are not particularly destructive, and when they do occur, they adjust the vortex to a new shape which can persist for long times.

Several avenues of further work present themselves. First, the class of tilted spheroidal vortices, examined by Miyazaki *et al.* (1999), exhibits similar linear instabilities; to date the nonlinear consequences of these instabilities have not been explored. However, it is likely that, as here, vortices will adjust to another near-ellipsoidal form which can persist for long times. Secondly, tilted ellipsoidal vortices are exact time-dependent solutions of the quasi-geostrophic equations (Meacham 1992), but for unequal axis lengths they nutate as well as rotate, generally at different frequencies (nearly all irrationally related). It may be of interest to examine their stability with respect to non-ellipsoidal disturbances by a generalized Floquet analysis. Additional classes of ellipsoidal equilibria exist when a background straining flow is included. Their linear stability has been examined recently by Hashimoto *et al.* (1999), for two special two-dimensional straining flows (pure deformation and pure linear shear), and by McKiver (2003), in the general case (but on a sheet of the parameter space joined to spheroids in the limit of zero strain). The latter study concluded that non-ellipsoidal instabilities are extremely rare; however, the parameter space investigated does not connect with the freely rotating ellipsoids studied here (there is a fold in the parameter space at a critical strain value). Further work is required to understand the stability of this other sheet of solutions in parameter space (a part of which has been explored by Hashimoto *et al.* 1999).

The quasi-geostrophic model used here is the simplest possible and the only one known to admit exact ellipsoidal vortex solutions. This model is applicable to oceanic dynamics and, to a degree, atmospheric dynamics. However, the compressibility of the atmosphere, with density ρ decaying almost exponentially with height as $\mathrm{e}^{-z/H}$ (here $H \approx 7\,\mathrm{km}$ is the 'scale height'), changes the inversion operator in (2.3) to

$$\nabla^2\psi - \frac{1}{H}\psi_z = q,$$

and this modifies the behaviour of vortices of height scales comparable to or greater than H (such vortices are widespread in the atmosphere). In particular, ellipsoidal vortices of uniform potential vorticity q are no longer exact solutions of the equations; preliminary results indicate that a vertical asymmetry appears in the analogous steadily rotating vortices, with the top of the vortex becoming more circular and the bottom becoming more eccentric (Scott & Dritschel 2005). This difference increases with total vortex depth, keeping H fixed, and is significant even for a vortex depth of $H/4$. A full exploration of the effects of compressibility requires finding the equilibria numerically, but assessing their stability appears to involve a straightforward extension of the methods used here.

Support for this research has come from the UK Natural Environment Research Council (grant NER/B/S/2002/00567).

REFERENCES

Chandrasekhar, S. 1969 *Ellipsoidal Figures of Equilibrium*. Dover, New York, 255 pp.

Dritschel, D. G. 1990 The stability of elliptical vortices in an external straining flow. *J. Fluid Mech.* **210**, 223–261.

Dritschel, D. G. 2002 Vortex merger in rotating stratified flows. *J. Fluid Mech.* **455**, 83–101.

Dritschel, D. G. & Ambaum, M. H. P. 1997 A contour-advective semi-Lagrangian algorithm for the simulation of fine-scale conservative fields. *Q. J. R. Met. Soc.* **123**, 1097–1130.

Dritschel, D. G., Reinaud, J. N. & McKiver, W. 2004 The quasi-geostrophic ellipsoidal vortex model. *J. Fluid Mech.* **505**, 201–223.

Dritschel, D. G. & de la Torre Juárez, M. 1996 The instability and breakdown of tall columnar vortices in a quasi-geostrophic fluid. *J. Fluid Mech.* **328**, 129–160.

Dritschel, D. G. & Viúdez, A. 2003 A balanced approach to modelling rotating stably stratified geophysical flows. *J. Fluid Mech.* **488**, 123–150.

Ebbesmeyer, C. C., Taft, B. A., McWilliams, J. C., Shen, C. Y., Riser, S. C., Rossby, H. T., Biscaye, P. E. & Östlund, H. G. 1986 Detection, structure, and origin of extreme anomalies in a Western Atlantic oceanographic section. *J. Phys. Oceanogr.* **16**, 591–612.

Garrett, C. 2000 *The Dynamic Ocean* (ed. G. K. Batchelor, H. K. Moffatt & M. G. Worster), pp. 507–553. Cambridge University Press.

Gill, A. E. 1982 *Atmosphere-Ocean Dynamics*. Academic, 662pp.

Hashimoto, H., Shimonishi, T. & Miyazaki, T. 1999 Quasigeostrophic ellipsoidal vortices in a two-dimensional strain field. *J. Phys. Soc Japan* **68**, 3863–3880.

Holton, J. R., Haynes, P. H., McIntyre, M. E., Douglass, A. R., Rood, R. B. & Pfister, L. 1995 Stratosphere–troposphere exchange. *Revs. Geophys.* **33**, 403–439.

Kerswell, R. R. 2002 Elliptic instability. *Annu. Rev. Fluid Mech.* **34**, 83–113.

Laplace, P. S. 1784 Théorie du Mouvement et de la Figure Elliptique des Planètes. Imprimerie de Ph-D Pierres, Paris, 153 pp.

McKiver, W. J. 2003 The motion of a quasi-geostrophic ellipsoidal vortex in a background shear flow. PhD thesis, St Andrews University.

McKiver, W. J. & Dritschel, D. G. 2003 The motion of a fluid ellipsoid in a general linear background flow. *J. Fluid Mech.* **474**, 147–173.

Meacham S. P. 1992 Quasigeostrophic, ellipsoidal vortices in stratified fluid. *Dyn. Atmos. Oceans* **16**, 189–223.

Miyazaki, T., Ueno, K. & Shimonishi, T. 1999 Quasigeostrophic tilted spheroidal vortices. *J. Phys. Soc Japan.* **68**, 2592–2601.

Moore, D. W. & Saffman, P. G. 1971 Structure of a line vortex in an imposed strain. In *Aircraft Wake Turbulence* (ed. J. H. Olsen, A. Goldburg & M. Rogers). Plenum.

Reinaud, J. N. & Dritschel, D. G. 2002 The merger of vertically offset quasi-geostrophic vortices. *J. Fluid Mech.* **469**, 287–315.

Reinaud, J. N., Dritschel, D. G. & Koudella, C. R. 2003 The shape of vortices in quasi-geostrophic turbulence. *J. Fluid Mech.* **474**, 175–191.

Reinaud, J. N. & Dritschel, D. G. 2005 The critical merger distance between two co-rotating quasi-geostrophic vortices. *J. Fluid Mech.* **522**, 357–381.

Scott, R. K. & Dritschel, D. G. 2005 Quasi-geostrophic vortices in compressible atmospheres. *J. Fluid Mech.* **530**, 305–325.

Siegel, A., Weiss, J. B., Toomre, J., McWilliams, J. C., Berloff, P. S. & Yavneh, I. 2001 Eddies and vortices in ocean basin dynamics. *Geophys. Res. Lett.* **28**, 3183–3186.

Zhmur, V. V. & Pankratov, K. K. 1990 Distant interaction of an ensemble of quasigeostrophic ellipsoidal eddies: Hamiltonian formulation. *Izv. Akad. Nauk. SSSR Phys. Atmos. Ocean* **26**, 972–981.

Zhmur, V. V. & Shchepetkin, A. F. 1991 Evolution of an ellipsoidal vortex in a stratified ocean: survivability of the vortex in flow with vertical shear. *Izv. Akad. Nauk. SSSR Phys. Atmos. Ocean.* **27**, 492–503.